

CHARACTERISATION OF AUSTENITIC 316LSi STAINLESS STEEL PRODUCED BY WIRE ARC ADDITIVE MANUFACTURING WITH INTERLAYER COOLING

C. R. Cunningham*, J. Wang[†], V. Dhokia*, A. Shrokani*, and S. T. Newman*

*Department of Mechanical Engineering, University of Bath, Bath, BA2 7AY

[†]Department of Architecture and Civil Engineering, University of Bath, Bath, BA2 7AY

Abstract

Wire arc additive manufacturing (WAAM) expands the possibilities of cost effectively producing large-scale, complex metal objects at high deposition rates. Austenitic stainless steel is a commonly used material and has many applications in the marine and nuclear industry due to its high toughness and corrosion resistance. Processes parameters such as heat input and interpass temperature can greatly affect the materials properties, part functionality and the economics of WAAM production. However, the effect of these process parameters is not well understood for WAAM of 316LSi. In this research, the effects of the interpass temperature and heat input process parameters on WAAM of austenitic AISI 316LSi stainless steel are experimentally analysed and evaluated. It was found that the heat input and interpass temperature influences the cellular/dendritic morphology and the formation of macro-scale grains within the microstructure. Additionally, use of higher heat input, resulted in a 28.7% improvement in average Young's modulus compared to lower heat input, although this remained lower than provided by wrought annealed material.

Keywords: *Wire arc additive manufacturing, Additive manufacturing, Interpass temperature, 316LSi, Directed energy deposition.*

Introduction

Wire Arc Additive Manufacturing (WAAM) is a directed energy deposition (DED) additive manufacturing approach [1] that uses an electric arc to melt metallic wire feedstock for the production of new parts or repair applications. Compared to other DED technologies that use electron beam or laser beam as a fusion source, the benefits of WAAM include the cost effectiveness of the process. This is due to the ability to source the open architecture equipment required for WAAM from a wide range of suppliers in the arc welding industry. Compared to powder-based additive manufacturing (AM) methods, the wire-based approach in WAAM offers the benefit of cheaper wire feedstock in many materials, and higher deposition efficiency [2]. Notable industrial applications of WAAM in recent years include the first additively manufactured metal bridge [3] and offshore crane hook [4].

Austenitic stainless steels find many applications within the marine, construction, nuclear industries due to its excellent corrosion resistance, adequate high temperature mechanical properties, formability and weldability [5]. Although AISI 316L has been intensively investigated as an AM material for powder bed fusion applications [6-11] and has been shown to show unexpectedly high combination of strength and ductility [12], exploration of the material characteristics has been comparatively limited for processing by WAAM. To date, a number of studies highlighted in table 1 have demonstrated that WAAM can achieve an ultimate tensile strength, yield stress and elongation in excess of cast material and in the region of that provided wrought annealed material across a range of WAAM process types [13-17].

Table 1 Material properties reported for AISI 316L categorised by WAAM process type, specimen orientation and interpass build strategy.

WAAM process type	Specimen orientation	Interpass build strategy – dwell duration	UTS (MPa)	YS (MPa)	EI (%)	Ref
GMAW ¹	Vertical	Fixed dwell – 2 min	533±23	235±6	48±2	[13]
GMAW-CMT ² continuous	Vertical	Fixed dwell - unspecified	547	336.9	42.0	[14]
	Horizontal		577.3	364.3	43.4	
GMAW-CMT pulsed	Vertical		536	331.7	45.6	
	Horizontal		588.0	374.0	45.1	
GTAW ³ -TopTIG	Vertical	100°C interpass temperature	539.9	322.2	43.1	[15]
	Horizontal		590.3	365.5	42.3	
GMAW-CMT	Vertical	Fixed dwell – 20 s	537.0	313.0	41%	[16]
	Horizontal		551.0	369.0		
GMAW – Speed Pulse	Horizontal	Fixed dwell – 20 s	550.0 ± 6	418.0	-	[17]
GMAW – Speed Arc	Horizontal	Fixed dwell – 20 s	553.0 ± 2	417.9	-	
GMAW	Vertical	Fixed dwell – 10 s	603.1	357.6	-	[17]
	Horizontal	Fixed dwell – 10 s	557.7	334.3	-	
	Vertical	Fixed dwell – 15 s	614.4	361.4	-	
	Horizontal	Fixed dwell – 15 s	605.4	340.7	-	
Wrought (annealed)	-	-	480	170	40	[18]
Cast	-	-	552	262	55	

¹ Gas Metal Arc Welding (GMAW)

² Cold Metal Transfer (CMT)

³ Gas Tungsten Arc Welding (GTAW)

To reliably produce high quality materials and ensure the consistent performance of AM materials in service, the process-structure-property relationship must be well understood [19]. It is also preferable for the desired material properties to be realised in-process due to enhancement of process efficiency. This is particularly beneficial for localized manufacture of large parts, or feature addition or repair applications where sizing and access to a heat treatment furnace might be an issue. To control the material microstructure and properties developed, suitable process parameters must be selected that provide a specific cooling rate, thermal gradient and solidification rate during the build [20].

The heat input from the welding torch, based on the current and voltage, directly influences the cooling rate experienced during a WAAM build. However, a range of heat input values are often possible whilst maintaining a stable melt pool and deposition geometry. The advantages of lower heat input in metal AM processes include a refined microstructure, which can translate to improved hardness and tensile strength. However, a decrease in residual stress-induced deflection is observed for increasing energy per unit length [21]. High levels of residual stress can have a detrimental effect on fatigue performance and corrosion resistance. Furthermore, higher residual stresses require more robust, and expensive fixturing to constrain the part during the build, the often-cited benefit of tool-less manufacture in additive manufacturing. Distortions that occur during the build, can reduce the quality of the deposition due to variation in contact tip distance. In addition, the volume of δ -ferrite is also affected by the cooling rate in AM. The volume δ -ferrite can be important to control due to its detrimental effect on pitting corrosion resistance [22]. Applications that require low magnetic permeability and high toughness at cryogenic temperatures may also require δ -ferrite to be controlled to acceptable levels through WAAM process.

The strategy employed for build temperature management can also affect the cooling rate and part quality. A fixed or time-variant dwell period may be used to set the inter-layer cooling time and prevent undesired heat accumulation that can destabilise the deposition geometry. Alternatively, an active cooling process may be used to increase the cooling rate post-deposition [23]. By increasing the interpass temperature a significant reduction in baseplate distortion was found for laser DED of Ti-6Al-4V control due to greater recrystallisation with associated dynamic reduction

of plastic strain and also stress relaxation at the higher build temperature [24]. As shown in table 1, in all cases a fixed or time variant interpass temperature dwell was used, indicating that this is an important aspect of WAAM 316L/LSi production. However, except for Wu et al. (2019) [17] where the effect of a small difference in dwell periods was considered, the effect of interpass dwell on the structure-property characteristics of the deposited material has not been explored.

The aim of this research study is to investigate the effect of heat input and interpass temperature on the WAAM location-specific material properties in relation to conventionally manufactured material.

Material fabrication

Thin-wall samples of length 150 mm and approximately 100 mm height as shown in Fig. 1 were produced in this study using a parallel path deposition strategy. Wire of type and 1 mm diameter was deposited onto 316L substrates of 50 mm × 200 mm × 6 mm dimension. The chemical composition of the wire and substrate is shown in table 2. Prior to commencing each build, the substrate surfaces were polished and then cleaned with acetone. The substrate was fixed during the WAAM build with bolts in each corner of the substrate.

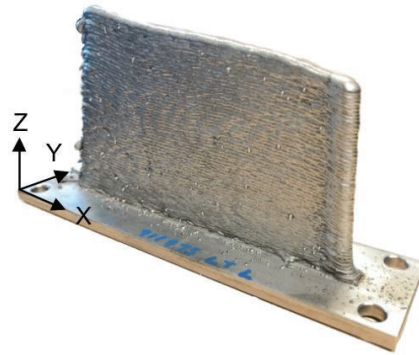


Figure 1 As-built geometry of 316LSi thin-walls and co-ordinate system.

Table 2 Chemical compositions of the wire and substrate used in the wire arc additive manufacture of the test samples.

	Cr	Ni	Mo	C	Mn	S	Si	N	Cu	Fe
Wire - 316LSi	18.250	12.070	2.530	0.008	1.600	0.0110	0.790	0.0320	0.083	Bal.
Substrate - 316L	17.010	10.107	2.152	0.023	1.232	0.0049	0.460	0.0507	-	Bal.

The factors of interpass temperature and heat input were investigated in a full factorial experimental design shown in table 3 with test walls built from process parameter combinations of low interpass temperature with low heat input (LIT-LHI), low interpass temperature with low heat input (LIT-LHI), high interpass temperature with high heat input (HIT-HHI), and high interpass temperature with low heat input (HIT-LHI). The heat input levels to be investigated were derived from the minimum and maximum travel speeds that could be achieved without excessive build-up of the weld bead or humping respectively to prevent any instabilities in deposition geometry during deposition and were achieved by varying the travel speed of the weld torch only. The upper level of interpass temperature was determined by the maximum temperature possible to achieve passively with continuous deposition for the lower heat input condition.

Table 3 Experimental wire arc additive manufacturing build parameters.

Experiment Ref.	Interpass temperature (°C)	Heat Input (kJ/mm)	Travel speed (mm/s)
LIT-HHI	50 (LIT)	0.47 (HHI)	2.32
LIT-LHI		0.26 (LHI)	4.90
HIT-HHI	160 (HIT)	0.47 (HHI)	2.32
HIT-LHI		0.26 (LHI)	4.90

The build parameters were fixed throughout all of the experiments and the values are provided in table 4.

Table 4 Fixed wire arc additive manufacturing build parameters

Parameters	Values
Wire feed rate	2 m/min
Contact tip distance	7.5 mm
Shielding gas flow rate	20 L/min
Shielding gas composition	97.5%Ar/2.5%CO ₂
Welding angle	0°
Wire diameter	1 mm
Pulse type	Primary
Pulse frequency	5 Hz

The WAAM equipment consisted of an Aristo 4004i power supply and wire feeder (ESAB Group (UK) Ltd), a fume extractor, controller and shielding gas supply configured as shown in Fig. 2. The weld torch cable which supplies the wire and shielding gas was routed through the WAAM enclosure, where it was affixed to the final motion system stage along with a pyrometer (Micro-Epsilon, CTM-2CF75-C3). The pyrometer provided continuous feedback of the surface temperature 30 mm in front of weld torch in the travel direction and was driven to the weld start point between passes to monitor the interpass temperature. The temperature readings were calibrated with a k-type thermocouple, and accuracy of the readings was monitored at regular intervals throughout the experimental builds.

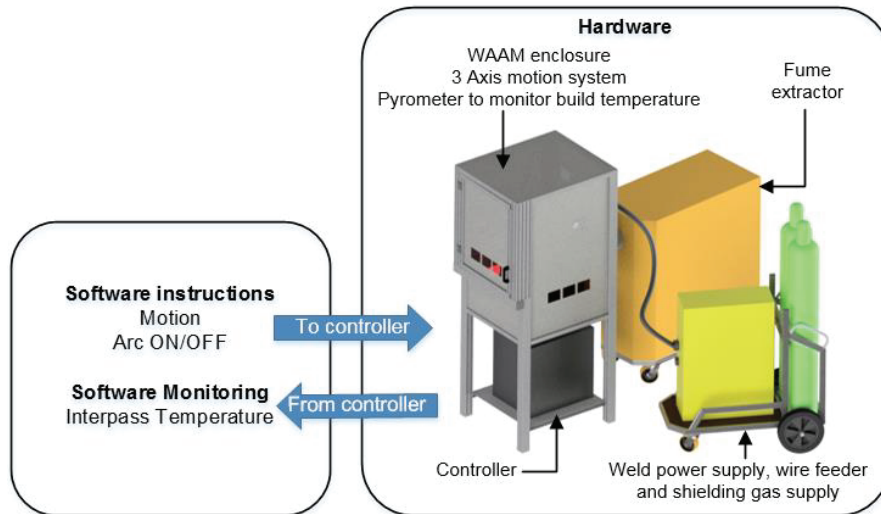


Figure 2 WAAM experimental set up.

Materials Analysis

To examine the microstructure through the build height of the experimental thin-walls, a section of 4 mm thickness was extracted from the location shown in Fig. 3 using a conventional band-saw. These sections were polished mechanically with SiC from grit number 400 to 4000, and subsequently polished with 0.5 μ m colloidal silica. A chemical etch using Marble's reagent solution (4g CuSO₄, 20ml HCl, and 20ml H₂O) was performed for 10 s to provide contrast between the γ -austenite and δ -ferrite phases. The YZ surface of each specimen was examined using an optical microscope and scanning electron microscope (SEM) (JEOL JSM-6480LV) was used to analyse the fracture surfaces of the tensile specimens. To investigate the variation in phase content and morphology in each sample, images were made at a magnification x 1000 with a spatial scanning frequency of 1 mm along the build height in YZ. These images were converted to binary using ImageJ and the ratio of white to black pixels recorded representative of the γ -austenite to δ -ferrite content respectively

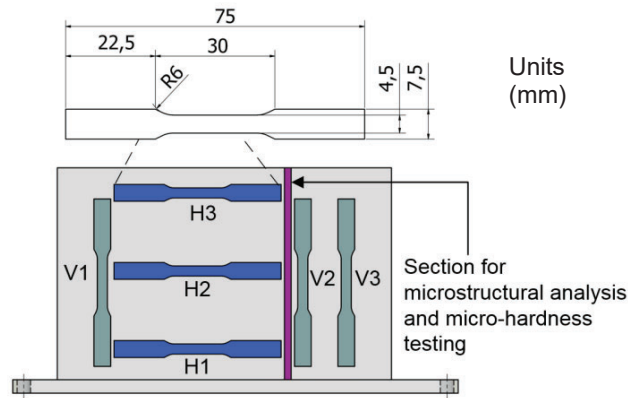


Figure 3 Orientation of tensile specimens within the WAAM experimental walls and specimen dimensions

The tensile coupon specimens were water jet cut from the experimental thin-walls in the orientations as shown in Fig. 3. The specimen dimensions were specified in accordance to ASTM E8 [25], with all specimens CNC machined to a uniform thickness of 3.3 mm. Uniaxial tensile tests were performed at room temperature using an Instron 3369 50 kN load cell with a clip gauge extensometer to study the plastic deformation behaviour on the macroscopic scale. The extension strain rate used was 0.00007 s⁻¹ in the elastic deformation region, followed by 0.00024 s⁻¹ upon transition to plastic deformation.

The experimental data was processed to determine the Young's modulus, yield strength, the ultimate tensile strength and fracture elongation. The Young's modulus was determined by considering the linear part of the stress-strain curve, and the yield strength adopted the 0.2% proof stress. Statistical analyses were carried out to identify significant effects and interactions via three-way analysis of variance (ANOVA) tests using Minitab® 18 software. The factors considered were the interpass temperature, heat input (quantitative factors) and specimen orientation (categorical factor). Main effects and interactions were determined to be significant if p-value was less than 0.05. The data was also checked for violations of normality and equivalence of variance as required for performing ANOVA.

The variation in micro-hardness throughout the build height was established with Vickers micro-hardness test equipment (Leco M400) with the same samples that were used to examine the

microstructural properties In accordance the ISO 6507-1 [26], a load of 500 g was applied for 10 s, with the first indentation located 3 mm inwards from the bottom surface of substrate and at the centreline of the WAAM layers. Subsequent measurements were made along the sample in increments of 1 mm in the build height direction.

The distortion of the substrates following release from the build fixture was captured using a ROMER Absolute scanning arm (Hexagon Manufacturing Intelligence, UK) and Geomagics Wrap® software (3D Systems Inc). The data was processed to obtain the profile of maximum deformation in the XZ and YZ planes.

Microstructure and periodicity

The LIT-LHI and HIT-HHI thin-wall specimens showed large irregularly shaped columnar macro-grains which grew across the layer bands in the build direction (BD) as shown in Fig 4. The LIT-LHI columnar grains displayed the greatest aspect ratio due to the strong thermal gradient developed by the combination greater inter-layer cooling and low heat input deposition. The reduced melt-pool temperature also minimizes the time for heterogeneous nucleation to occur ahead of the solidification front, encouraging epitaxial growth dominant along the $\langle 100 \rangle$ easy growth direction due to the strong thermal gradient. The HIT-HHI thin-wall specimen, experienced the most elevated build temperatures and consequently had a strong tendency for grain growth [27]. However, with less directional heat transfer along the build height, more diverse competitive grain growth was able to occur, reducing the length and aspect ratio of the grains that formed to impart a less extreme texture.

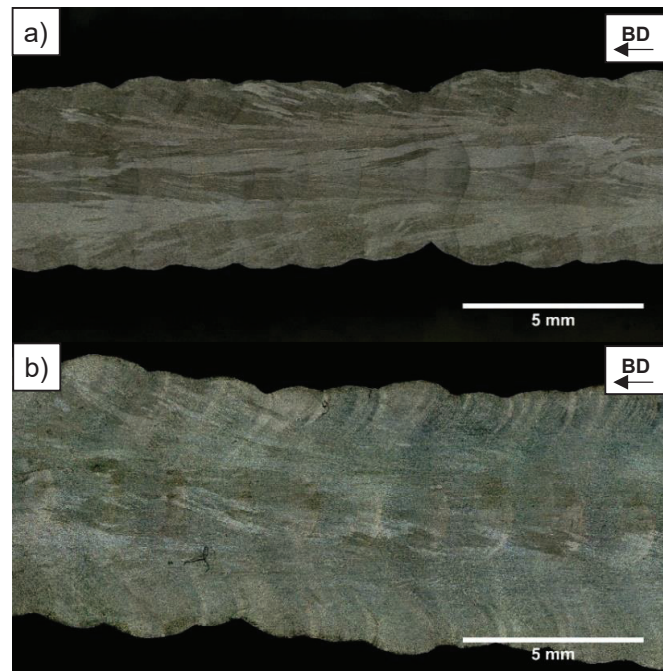


Figure 4 Columnar grain growth visible through the macro-structure in a) LIT-LHI and b) HIT-HHI experimental thin walls.

The as-built cross section morphologies of the banding zones at 15 mm from the bottom of the substrate are shown in Fig. 5, respectively for each of the experimental thin-walls. It was evident from each of the experiments that the δ -ferrite developed was of dendritic morphology within an austenite matrix. Three periodic zones are visible, including a fine grain zone (FZ) immediately to

the left of the re-melt banding line caused by recrystallisation. This was primarily lathy δ -ferrite morphology, although for HIT-HHI and LIT-LHI cellular regions were also observed. The transition zone (TZ) displayed a progressive coarsening of this FZ microstructure due to increasing re-heat effect from the superimposed layers in this direction and conversely a progressive refinement of the coarse grain zone (CZ) due to diminishing re-heat effect. The CZ was positioned to the right of the re-melt banding line, received the most re-heat without re-melting and was subsequently of the most coarsened vermicular morphology.

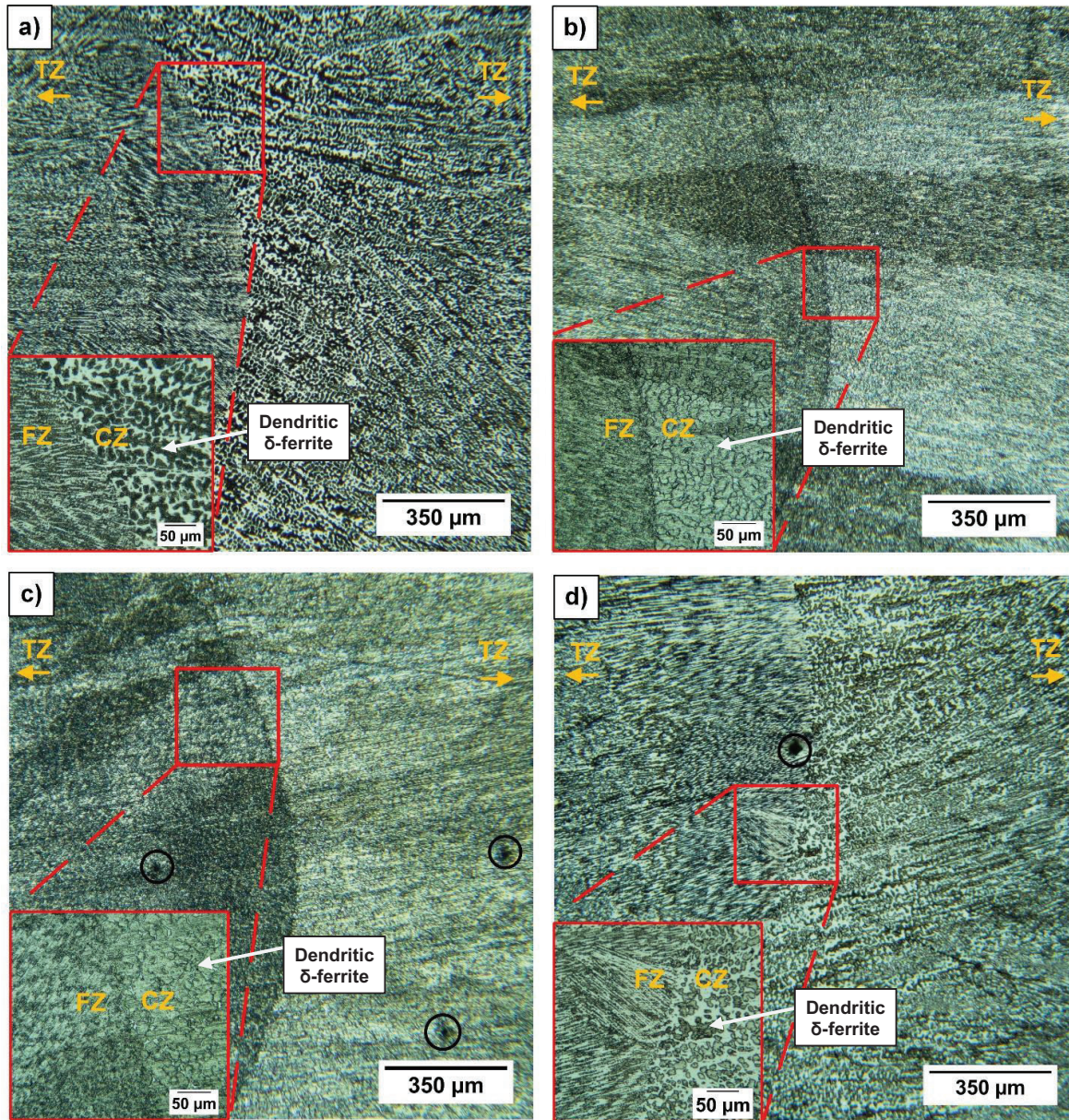


Figure 5 Experimental thin wall morphologies at the banding zone 15mm from the bottom of the substrate for a) LIT-HHI b) LIT-LHI, c) HIT-HHI d) HIT-LHI. Note: Vickers Micro-hardness indentations are visible in c) and d) are circled in black.

The δ -ferrite network within LIT-HHI (Fig 5a inset) was observed to be more extensive with larger primary dendrite arm length, whereas the δ -ferrite is discontinuous in CZ of the HIT-LHI (Fig 5d inset). This indicated that greater decomposition of δ -ferrite occurred, possibly due to greater reheating effect due to reduced layer height or increased interpass temperature. It is known that

vermicular δ -ferrite morphology transforms to fine short ferrite precipitates when subject to repeated repair welding of 316L [28]. The similarity of the process to WAAM and the lengthy re-heat distance for HIT-HHI can explain the relatively fine microstructure observed within the macroscale grains. As the morphology within the FZ of LIT-LHI could not be observed clearly with optical microscopy, this sample was analysed with SEM. As shown in Fig. 6, colonies of cells were present which were grouped into sub-grains, with a sub-grain boundary highlighted. Lathy dendritic primary arm δ -ferrite could be observed within the fine cellular austenitic matrix.

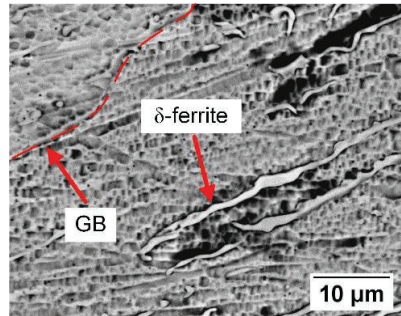


Figure 6 SEM (BEI) micrograph of 85mm build height of LIT-LHI showing the lathy δ -ferrite within cellular austenite and a sub-grain boundary.

The LIT-LHI and HIT-HII demonstrated the most consistent average white pixel concentration along the built height as shown in Fig. 7, which was attributed to the more refined and homogeneous morphology between the CG, TZ and FZ for these samples. Overall, the LIT-LHI displayed the greatest volume of δ -ferrite which was expected due to the high cooling rate achieved with the combination of low heat input and interpass temperature. These conditions would lead to the most retained metastable δ -ferrite and least opportunity for decomposition through the reheat cycles.

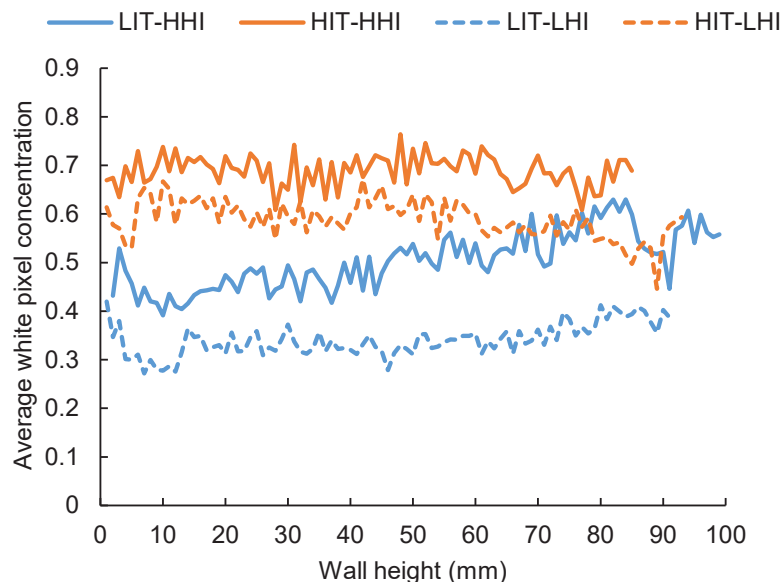


Figure 7 Average white pixel concentration along the WAAM experimental wall height. Etching and the converting to binary process resulted in austenite = white, δ -ferrite = black.

Mechanical properties and deformation behavior

The tensile properties of AISI 316LSi samples fabricated by WAAM were evaluated as shown in table 5 with the data are expressed as mean \pm standard deviation from sample group number, n.

Table 5 Young's modulus, yield strength, ultimate tensile strength, and elongation of the investigated as-built materials including standard deviation within sample group of size, n.

Experiment ref.	Specimens	n	Young's modulus (GPa)	Yield Strength (MPa)	Ultimate Tensile Strength (MPa)	Elongation (%)
LIT-HHI	Average	6	179.2 \pm 42.7	320.2 \pm 26.9	570.9 \pm 22.1	42.1% \pm 2.3
	Horizontal	3	192.0 \pm 50.6	330.7 \pm 34.4	582.2 \pm 21.4	42.0% \pm 2.9
	Vertical	3	166.5 \pm 38.9	309.8 \pm 17.08	559.6 \pm 19.5	42.2% \pm 2.2
LIT-LHI	Average	6	121.2 \pm 16.3	308.1 \pm 16.6	561.2 \pm 32.6	41.4% \pm 8.6
	Horizontal	3	130.1 \pm 19.1	313.8 \pm 14.8	549.4 \pm 34.5	47.3% \pm 8.6
	Vertical	3	112.2 \pm 7.7	302.4 \pm 19.2	572.9 \pm 32.5	35.5% \pm 2.9
HIT-HHI	Average	6	165.4 \pm 42.0	302.6 \pm 25.0	579.0 \pm 29.9	44.1% \pm 5.2
	Horizontal	3	162.6 \pm 50.1	302.0 \pm 11.4	576.7 \pm 10.2	47.0% \pm 5.9
	Vertical	3	168.2 \pm 43.4	303.1 \pm 37.9	581.4 \pm 46.0	41.3% \pm 3.0
HIT-LHI	Average	6	141.3 \pm 26.9	298.8 \pm 5.5	565.2 \pm 9.43	43.0% \pm 4.8
	Horizontal	3	134.0 \pm 20.3	300.1 \pm 5.4	551.9 \pm 10.2	44.4% \pm 5.5
	Vertical	3	148.6 \pm 35.1	297.5 \pm 6.8	578.4 \pm 26.5	40.9% \pm 4.1

The statistical analyses revealed that orientation of the specimens has a significant effect ($p=0.018$) on the elongation properties of the as-built material. The horizontal specimens provided an average elongation of 45.2% compared to 40.0% provided by the vertical specimens. This indicates that on average the specimens extracted in the horizontal orientation provide greater ductility. Previous studies investigating ductility of 316L have shown that when more grain boundaries are encountered, higher strength and lower elongation are expected [29]. A higher number of grain boundaries and lower elongation are expected in horizontal specimens due to directional grain growth, suggesting that another mechanism is providing the additional ductility in WAAM horizontal specimens. The heat input was found to have a significant effect on the Young's modulus, with high heat input providing an average of 164.3GPa, compared to low heat input with an average of 127.7GPa. This could be significant for high strength applications as in both cases plastic deformation would proceed at a lower load than for wrought annealed material. Besides Young's modulus and elongation, the other mechanical properties investigated generally exceed that provided by wrought annealed material.

As identified in other research by Yang et al. [30], there is a general decrease in micro-hardness with increasing distance from the substrate. The high heat input level with high interpass temperature substantially reduced the micro-hardness for the start section of build height compared to the same heat input with longer cooling between passes. In contrast, for the low heat input samples there was little difference in start section micro-hardness for both interpass temperatures. This is reflected in the similarity of the microstructure as shown in Fig. 8 and is explained by the limited heat accumulation in the high interpass temperature at the start of the build. As the build proceeds, the effect of the high interpass temperature becomes more apparent with the low heat input experiments, with the high interpass temperature negatively impacting on the micro-hardness within the top section of the build height. This indicates that selection of an appropriate interpass temperature is important to maintain micro-hardness properties and reducing micro-hardness heterogeneity in the build direction for high heat input WAAM build strategies.

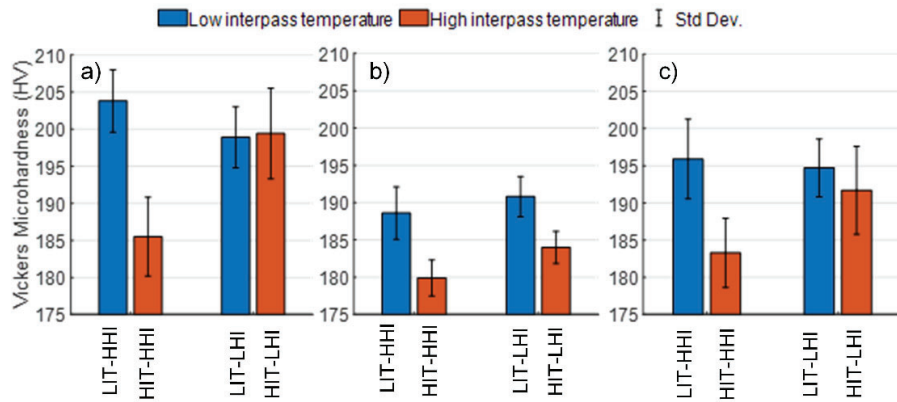


Figure 8 Vickers micro-hardness of a) first 25mm of the wall height b) last 25mm of wall height c) average of both sections

Fractography

Fracture surfaces were observed by SEM and the representative images are reported in Fig. 9. The specimens all show typical fracture features of ductile materials, with small dimples of less than 1 μm in diameter visible throughout the surface.

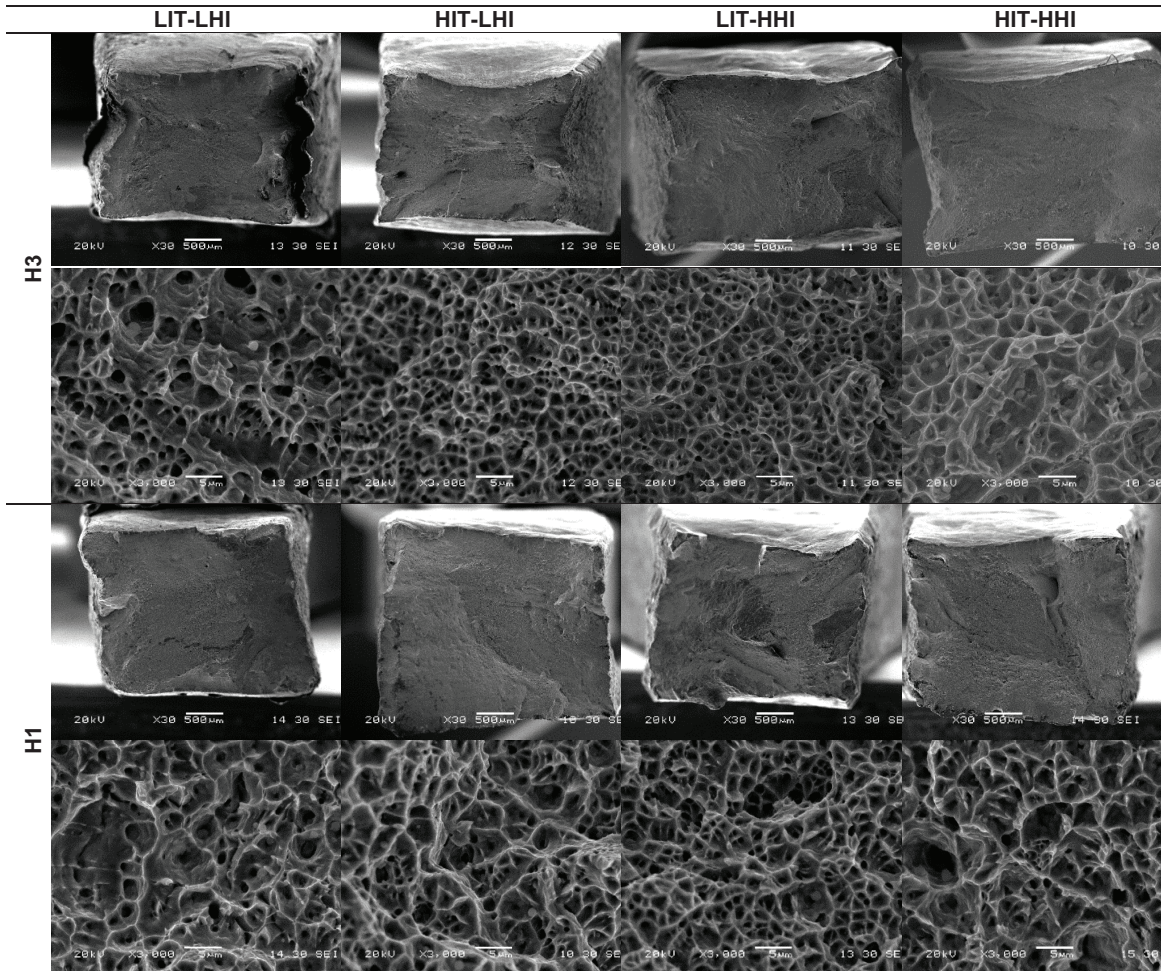


Figure 9 SEM micrographs of the surface of the fractured tensile specimens

Whilst no significant differences in the morphology of dimples could be observed between the experimental test conditions, the low interpass temperature with the high heat input condition (LIT-HHI) appeared to reduce the dimple diameter compared to the high interpass temperature condition. Future work will explore possible correlations of dimple size and frequency, with the tensile properties of 316LSi produced by WAAM for each of experimental test conditions investigated in this research.

Distortion

The profile of maximum distortion in the XZ and YZ planes for each wall are shown in Fig. 10. It can be seen that in the XZ plane, a high interpass temperature can reduce the residual stress induced distortion by a small amount, with the greatest improvement seen for high heat input experiments. Reduction in distortion was also found with increased interlayer cooling time for the lower heat input experiments in the YZ plane. However, the results are less conclusive for high heat input condition where the high interpass temperature distortion (HIT-HHI) exceeds that of the low interpass temperature (LIT-HHI) on one side of the YZ plane. This indicates that a high interpass temperature build strategy may not be as effective at reducing distortion for the YZ plane with higher levels of heat input.

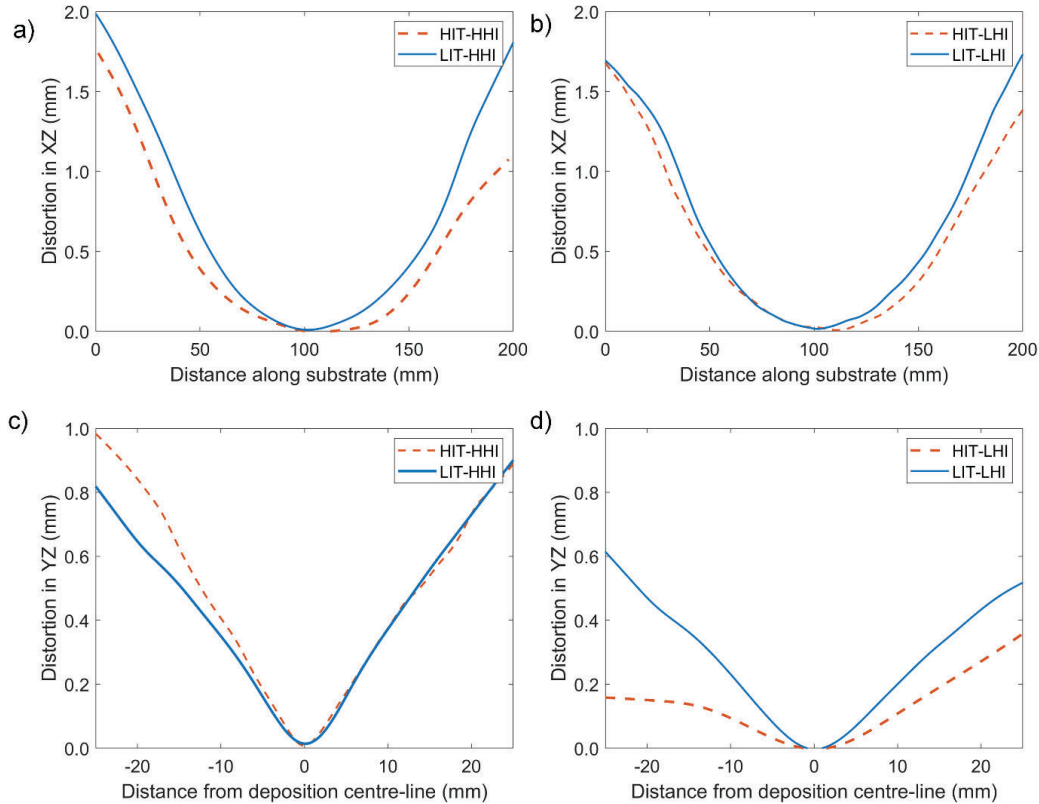


Figure 10 Maximum distortion profiles in the XZ plane for
a) HIT-HHI and LIT-HHI b) HIT-LHI and LIT-LHI and in YZ plane for c) HIT-HHI and LIT-HHI d) HIT-LHI and LIT-LHI.

Conclusions

This paper has experimentally investigated the effect of heat input and interpass temperature on the microstructure, hardness, tensile strength, and stiffness for stainless steel 316LSi walls manufactured by WAAM identifying the following new findings and conclusions:

1. The microstructures of AISI 316LSi produced by WAAM generally consisted of a mixture of fine columnar dendrites and isolated cellular regions. The microstructures varied periodically across the layer bands, with fine, transitional and coarse grain regions.
2. The inter-layer cooling time between layers affected the development of macro-scale grain structures within the microstructure. These exceeded 5 mm with the low interpass temperature and low heat input condition. Macro-scale grains were also observed with the high interpass temperature with high heat input experiment however, these were more equiaxed which was attributed to break-down by competitive grain growth.
3. The heat input was found to have a significant effect on the Young's modulus of AISI 316LSi produced by WAAM with high heat input processing parameter providing an average of 164.3GPa, compared to low heat input with an average of 127.7GPa.
4. The tensile specimens extracted in the horizontal orientation provide statistically significant greater ductility, with an average elongation of 45.2% compared to 40.0% provided by the vertical specimens.
5. Inter-layer cooling time influences the distortion of WAAM produced parts, with results indicating that a higher interpass temperature could be used to reduce the residual stress induced distortion of the substrate, although further research is required.

Acknowledgements

The authors would like to acknowledge support from Renishaw PLC (EPSRC CASE studentship No. 1780168).

References

- [1] *ASTM F3187-16, Standard Guide for Directed Energy Deposition of Metals*, 2016.
- [2] A. Nycz, A. I Adediran, M. W. Noakes, and L. J. Love, "Large Scale Metal Additive Techniques Review," *Solid Freeform Fabrication 2016: Proceedings of the 26th Annual International Solid Freeform Fabrication Symposium – An Additive Manufacturing Conference*, pp. 2001-2006, 2016.
- [3] MX3D. (2019, 26th June 2019). *MX3D Bridge*. Available: <https://mx3d.com/projects/bridge-2/>
- [4] Huisman. (2019). *Huisman successfully load tests world's first 3d printed offshore crane hook*. Available: https://www.huismanequipment.com/en/media_centre/press_releases/news_item/110/Huisman-successfully-load-tests-world-s-first-3d-printed-offshore-crane-hook
- [5] Z. Brytan, W. Borek, and T. Tański, "Introductory chapter: Why austenitic stainless steels are continuously interesting for science?," *IntechOpen, Austenitic Stainless Steels - New Aspects*, 2017.
- [6] M. Shamsujjoha, S. R. Agnew, J. M. Fitz-Gerald, W. R. Moore, and T. A. Newman, "High Strength and Ductility of Additively Manufactured 316L Stainless Steel Explained," (in English), *Metallurgical and Materials Transactions a-Physical Metallurgy and Materials Science*, 49a (7): 3011-3027, 2018.
- [7] T. Simson, A. Emmel, A. Dwars, and J. Böhm, "Residual stress measurements on AISI 316L samples manufactured by selective laser melting," *Additive Manufacturing*, 17:183-189, 2017.
- [8] G. Sander, S. Thomasa, V. Cruza, M. Jurga, N. Birbilisa, X. Gaoa, M. Brameld, and C. R. Hutchinsona, "On The Corrosion and Metastable Pitting Characteristics of 316L Stainless Steel Produced by Selective Laser Melting," *Journal of the Electrochemical Society*, 164(6):C250-C257, 2017.

- [9] W. E. King, , H. D. Barth, V. M. Castollo, G. F. Gallegos, J. W. Gibbs, D. H. Hahn, C. Kamath, and A. M. Rubenchik, "Observation of keyhole-mode laser melting in laser powder-bed fusion additive manufacturing," *Journal of Materials Processing Technology*, 214(12): 2915-2925, 2014.
- [10] S. A. Khairallah, A. T. Anderson, A. Rubenchik, and W. E. King, "Laser powder-bed fusion additive manufacturing: Physics of complex melt flow and formation mechanisms of pores, spatter, and denudation zones," *Acta Materialia*, 108, 36-45, 2016.
- [11] Y. Zhong, L. Rannar, L. Liu, A. Koptug, S. Wilman, J. Olsen, D. Cui, and Z. Shen, "Additive manufacturing of 316L stainless steel by electron beam melting for nuclear fusion applications," *Journal of Nuclear Materials*, 486:234-245, 2017.
- [12] M. S. Pham, B. Dovgvy, and P. A. Hooper, "Twinning induced plasticity in austenitic stainless steel 316L made by additive manufacturing," *Materials Science and Engineering: A*, 704: 102-111, 2017.
- [13] X. H. Chen, J. Li, X. Cheng, B. He, H. M. Wang, and Z. Huang, "Microstructure and mechanical properties of the austenitic stainless steel 316L fabricated by gas metal arc additive manufacturing," (in English), *Materials Science and Engineering a-Structural Materials Properties Microstructure and Processing*, 703: 567-577, Aug 4 2017.
- [14] N. Rodriguez, L. Vázquez, I. Huarte, E. Arruti, I. Tabernero, and P. Alvarez, "Wire and arc additive manufacturing: a comparison between CMT and TopTIG processes applied to stainless steel," *Welding in the World*, 62(5): 1083-1096, 2018.
- [15] A. Queguineur, G. Rückert, F. Cortial, and J. Y. Hascoët, "Evaluation of wire arc additive manufacturing for large-sized components in naval applications," *Welding in the World*, 62(2):259-266, 2017.
- [16] L. Wang, J. Xue, and Q. Wang, "Correlation between arc mode, microstructure, and mechanical properties during wire arc additive manufacturing of 316L stainless steel," *Materials Science and Engineering: A*, 751:183-190, 2019.
- [17] W. Wu, J. Xue, L. Wang, Z. Zhang, Y. Hu, and C. Dong, "Forming Process, Microstructure, and Mechanical Properties of Thin-Walled 316L Stainless Steel Using Speed-Cold-Welding Additive Manufacturing," *Metals*, 9(1): 109, 2019.
- [18] ASM International, *Metals Handbook. 9th Ed. Vol. 3. Properties and Selection Stainless Steels, Tool Materials & Special-purpose Metal*. ASM, 1980.
- [19] T. DebRoy, H. L. Wei, J. S. Zuback, T. Mukherjee, J. W. Elmer, J. O. Milewski, A. M. Beese, A. Wilson-Heid, A. De, and W. Zhang, "Additive manufacturing of metallic components – Process, structure and properties," *Progress in Materials Science*, 92: 112-224, 2018.
- [20] W. J. Sames, F. A. List, S. Pannala, R. R. Dehoff, and S. S. Babu, "The metallurgy and processing science of metal additive manufacturing," *International Materials Reviews*, 61(5): 315-360, 2016.
- [21] A. S. Wu, D. W. Brown, M. Kumar, G. F. Gallegos, and W. E. King, "An Experimental Investigation into Additive Manufacturing-Induced Residual Stresses in 316L Stainless Steel," *Metallurgical and Materials Transactions A*, 45(13): 6260-6270, 2014.
- [22] C. D. Lundin, W. T. Delong, and D. F. Spond, "Ferrite-Fissuring Relationship in Austenitic Stainless-Steel Weld Metals," (in English), *Welding Journal*, 54(8): S241-S246, 1975.
- [23] P. Henckell, K. Günther, Y. Ali, J. P. Bergmann, J. Scholz, and P. Forêt, "The Influence of Gas Cooling in Context of Wire Arc Additive Manufacturing—A Novel Strategy of Affecting Grain Structure and Size," in *TMS 2017 146th Annual Meeting & Exhibition Supplemental Proceedings*, M. The Minerals and S. Materials, Eds. Cham: Springer International Publishing, 2017, 147-156.
- [24] E. R. Denlinger, J. C. Heigel, P. Michaleris, and T. A. Palmer, "Effect of inter-layer dwell time on distortion and residual stress in additive manufacturing of titanium and nickel alloys," (in English), *Journal of Materials Processing Technology*, 215: 123-131, 2015.
- [25] *ASTM E8/E8M, Standard Test Methods for Tension Testing of Metallic Materials*, 2013.
- [26] *BS EN ISO 6507-1, Metallic materials – Vickers hardness test Part 1: Test method (ISO 6507-1:2018)*.
- [27] K. Saeidi and F. Akhtar, "Subgrain-controlled grain growth in the laser-melted 316 L promoting strength at high temperatures," *R Soc Open Sci*, 5(5): 172394, 2018.
- [28] I. AghaAli, M. Farzam, M. A. Golozar, and I. Danaee, "The effect of repeated repair welding on mechanical and corrosion properties of stainless steel 316L," *Materials & Design (1980-2015)*, 54: 331-341, 2014.

- [29] Y. Zhong, "Sub-Grain Structure in additive manufactured SS316L," PhD thesis, Department of Materials and Environmental Chemistry, Stockholm University, 2017.
- [30] N. Yang, J. Yee, B. Zheng, K. Gaiser, T. Reynolds, L. Clemon, W. Y. Lu, J. M. Schoenung, and E. J. Lavernia, "Process-Structure-Property Relationships for 316L Stainless Steel Fabricated by Additive Manufacturing and Its Implication for Component Engineering," *Journal of Thermal Spray Technology*, 26(4): 610-626, 2016.